From Cells to Laminate: Probing and Modeling Residual Stress Evolution in Thin Silicon Photovoltaic Modules using Synchrotron X-ray Micro-diffraction Experiments and Finite Element Simulations

Sasi Kumar Tippabhotla[1], Ihor Radchenko[1], Wenjian Song[1], G. Illya[2], V. Handara[1], M. Kunz[3], N. Tamura[3], Andrew A. O. Tay[1,a], A. S. Budiman[1,b*]

[1]Singapore University of Technology and Design, Singapore 487372
[a]Formerly of National University of Singapore, Singapore,
[b]Formerly of SunPower Corporation, R&D, San Jose, CA 95134.

[2]Center for Solar Photovoltaics Materials & Technology (CPV)
Surya University, Tangerang, Indonesia 15810.

[3]Advanced Light Source (ALS)
Lawrence Berkeley National Laboratory (LBNL), Berkeley, CA 94720.

*suriadi@alumni.stanford.edu

Abstract

High stress and fracture of silicon crystalline solar cells has recently been observed in increasing percentages especially in solar photovoltaics (PV) modules involving thinner silicon solar cells (<200 um). Many failures due to fracture of cells have been reported from the field and handling. However, a significantly higher number of failures have also been reported during module integration (soldering/ stringing and lamination) indicating a PV laminate/module with significantly high residual stresses and hence more prone to cell fractures. We characterize the residual stress evolution in crystalline silicon solar cells during module integration process, which is the current knowledge gap. The residual stress characterization was achieved through a systematic research using synchrotron X-ray submicron diffraction experiments coupled with physics-based Finite Element modeling of the PV module integration process. Thought this work we also demonstrate the unique capability of Synchrotron X-ray submicron diffraction to quantitatively probe residual stress in encapsulated silicon solar cells that has ultimately enabled these findings leading to the enlightening of the role of soldering and encapsulation processes. While our experiments quantify the stress at different process states including encapsulated cells, our FEA simulations, for the first time unravel the physical reasoning for the stress evolution and expected to bridge the

knowledge gap. This model can be further used to suggest methodologies that could lead to lower stress in encapsulated silicon solar cells, which are the subjects of our continued investigations.

1. Introduction

In photovoltaic (PV) modules, made of crystalline silicon solar cells, cracking of silicon near soldered metallic interconnects has been widely observed and reported [1-5]. In the module-making process, cells (both generic and back contact, Figure 1a) will be first interconnected with soldered copper ribbons (at ~ 220^0 C) as illustrated in Figure 1b. Subsequently laminated (at ~ 150^0 C) with other constituent materials of different coefficients of thermal expansion (CTE) as illustrated in Figure 1c. to form the modules. At these high temperatures of soldering and Encapsulated (also called lamination), due to mismatch of CTE, constituent materials tend to develop differential thermal strain and thus high residual stress. These internal residual stresses are detrimental to the reliability of the solar cells and modules as they act as stress localization centers and initiate cracking and failure during the operation of the module [1- 5]. Further, with the thinning of the silicon wafer to reduce cost of the silicon solar cell modules, the silicon cell becomes even more susceptible to cracking due to higher residual stresses [2-3]. The mechanics of stress evolution in the silicon cells during module fabrication needs to be thoroughly understood in order to reduce stress, improve the design life and reliability of the solar PV modules incorporating thinner silicon cells.

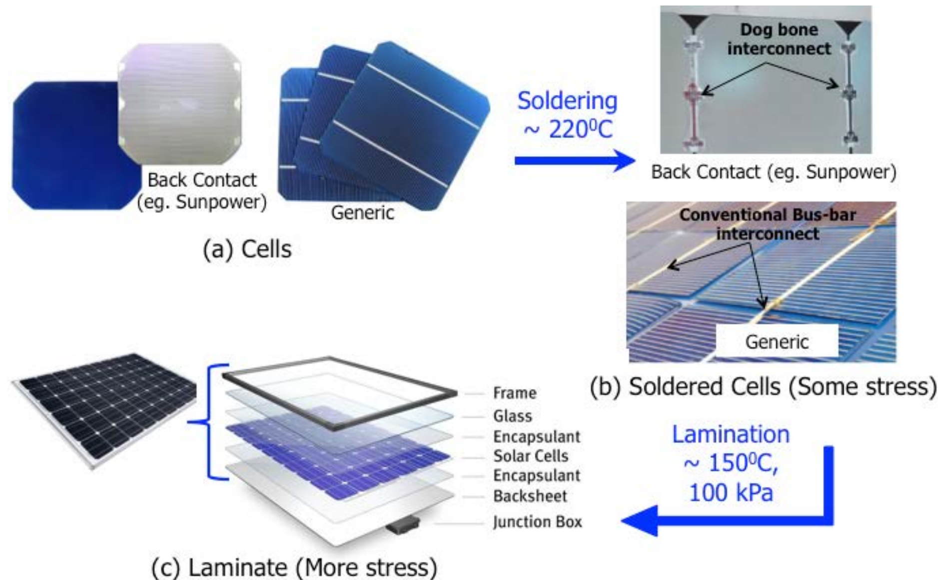

Figure 1: Journey of typical silicon cells in solar PV module integration process (All the pictures were taken from public domain)

Researchers have used different experimental and numerical simulations to evaluate the residual thermal stress due to soldering and lamination, and stresses due to operational loads [4-16]. Gabor et al. [4] and Wendt et al. [5] used analytical methods to

evaluate soldering-induced stresses. Chen et al. [6] used finite element analysis (FEA) to simulate residual stress and bow of the cell due to soldering and showed that thinner cells crack due to high stress during soldering. Dietrich et al. [7] used FEA and experiments to investigate different metallization layouts and their effect on cell stress through simulation and bending tests on single modules with 5 cell strings. Their findings conclude that neglecting soldering induced stresses will lead to incomplete fracture characterization of encapsulated cells. Sun et al. [8] used analytical modeling to calculate stresses due to lamination and thermal loading but this model did not consider cell stress / bow due to soldering. Lee and Tay [9-10] used FEA to determine thermal stresses induced in PV modules post-lamination and also during operation. Several other researchers have studied stresses due to lamination and thermo-mechanical loading using both FEA and experiments [11-16] but these studies either ignored effects of soldering in subsequent lamination process or considered only soldered state of the cells. Budiman et al. [17-19] demonstrated for the first time the use of a Synchrotron Scanning X-ray Micro-diffraction (μSXRD) to characterize the residual stress in the solar cells of PV laminates made of mono-crystalline silicon cells with back metallization technology. The μSXRD technique [17-19] was shown to be capable of quantifying the stress distribution in the encapsulated silicon solar cells. However this work did not provide any insights into how the stresses evolved or the causes. **This survey of the literature has clearly shown a knowledge gap as apparently, no reports have yet been made which show the stress evolution during complete module fabrication incorporating soldering and lamination processes sequentially. The residual stress and deformation induced in the silicon cells in a PV module is a result of sequential processing from soldering/stringing to encapsulation. The deformation and residual stress state in the cells after soldering forms the initial condition for the subsequent encapsulation process. Hence the final residual stress in the cells depends on this initial condition. In such a scenario, it is necessary to evaluate the residual stress at each step of module fabrication and investigate the physical reason behind change of stress, which is the fundamental objective of this work. Only such evaluation will provide insights in to the mechanics of the residual stress evolution in during module fabrication and help to characterize the effect of material and process parameters on it and help to optimize the PV modules for higher fatigue life and reliability. Furthermore, it will also help to identify and mitigate the major risk factors, currently being faced by the PV industry in sustaining the advanced technologies such as ultra-thin silicon cells, different encapsulation materials for cost reduction or changes in module fabrication processes for ease and cost reduction etc.**

In this manuscript, we quantify the residual stress distribution in crystalline silicon back-contact solar cells, post-soldering and post-encapsulation through our μSXRD experiments and for the first time provide insights into the evolution of the residual stress during the module integration process, starting from soldering to encapsulation. While our experiments quantify the stress at different process states, our FEA simulations provide physical reasoning for the stress evolution. **Our experiments and FEA simulations, explained in the following sections are expected to bridge the knowledge gap identified in the literature survey and help the PV industry to address the associated module reliability issues.**

2. Synchrotron Scanning X-ray Micro-diffraction (μSXRD) – Experimental Setup and Procedure

2.1 Introduction to Synchrotron X-ray Micro-Diffraction Beamline

Following Bragg's Law [20], the μSXRD technique utilizes a high-brilliance polychromatic X-ray radiation, generated by the synchrotron source, to characterize the crystal geometry of materials in the volume below the surface exposed to the X-ray beam [21]. It can be used to measure the crystal orientation, structure and, partially, its distortion (deviatoric strain) [22]. For the case of solar PV modules, unlike laboratory X-ray diffraction techniques, high-brilliance synchrotron X-ray beam can penetrate through its encapsulation and thin layers of metallization and reach the cell. Hence, we can observe the crystalline state of the encapsulated cell without damaging it mechanically [17-19]. Moreover, synchrotron X-ray beam can be focused to a submicron resolution thus allowing a high spatial resolution for the cell crystallographic characterization. High spatial resolution of μSXRD is essential to understand the distribution of residual stress in the cell, because the stress is highly localized and concentrated around the small areas near interconnects (Refs. [17-19], and as also confirmed again by our measurements in the present manuscript).

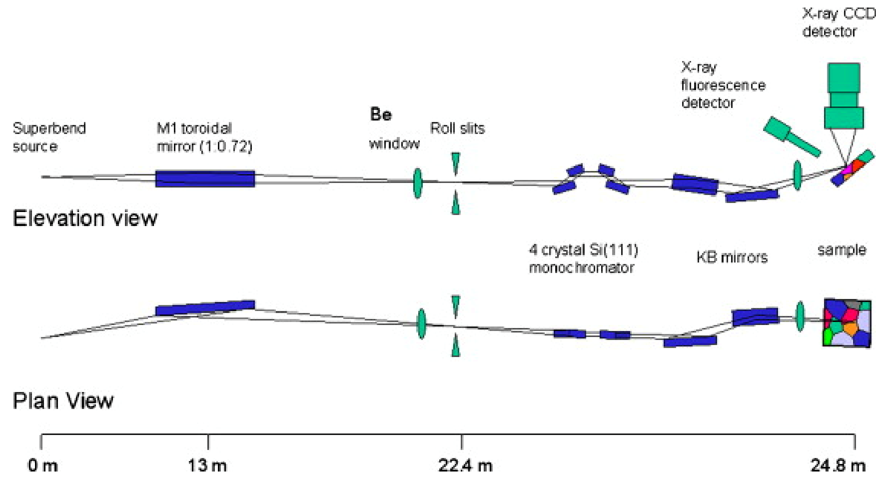

Figure 2: Elevation and plan view of the 12.3.2 microdiffraction beamline at the advanced light source (courtesy of M. Kunz et al. [24])

For our experiments, we have used the μSXRD setup in the beamline 12.3.2 [23-24] of Advanced Light Source (ALS), Lawrence Berkeley National Laboratory (LBNL), Berkeley, California, USA. A schematic of the beamline layout is shown in Figure 2. In the beamline, polychromatic X-ray beam of energy range from 5keV to 20keV is used. The beam is focused to a diameter of 0.8 μm. X-ray scattering is measured using a Pilateus 2D X-ray detector. **A monochromator is available in the setup, which can be engaged optionally to get a monochromatic beam of particular energy for energy scan or powder diffraction. In this work only polychromatic beam was used.** The beamline also allows an automatic raster scanning of the sample with single Laue pattern acquisition time below 1 sec. [23-26] Hence, Laue patterns for the points laying on the large area scan grid can be characterized within a reasonable time (for example, 1cm by 1cm area was scanned in ~7 hours using 100μm grid spacing). The orientation and deviatoric strain maps

for the scanned area can be constructed using the measured sequence of Laue patterns via XMAS software package as shown in Figure 3 [26]. Complete description about the technique in ALS, beamline 12.3.2 has been described elsewhere [23-26].

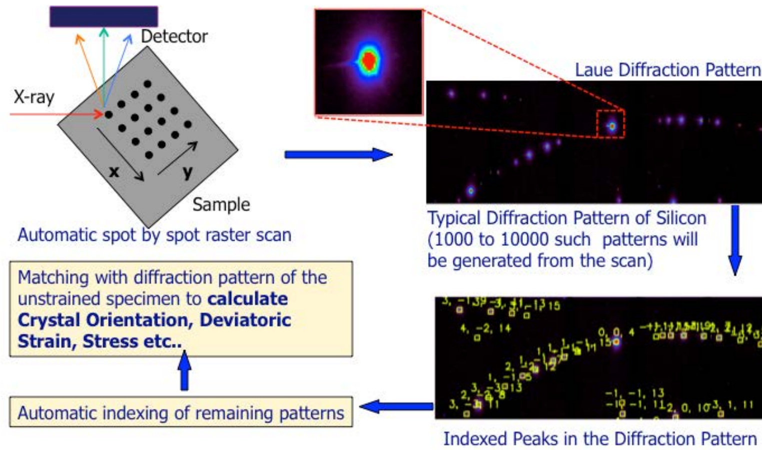

Figure 3: Typical Process Map of Automated μSXRD at ALS BL-12.3.2 and Subsequent Analysis using XMAS [26].

2.2 Experimental Sample Preparation and Procedure

The experiments performed in this work are aimed at quantifying the stress state in the crystalline silicon solar cells at different stages of the module-making process from cell stringing to encapsulation. A soldered string of two typical 125x125 mm mono-crystalline back-contact solar cells of thickness 180 μm, joined by a typical tin-coated copper interconnect as shown in Figure 4a was selected for the experiment. **The interconnect (thickness ~ 100 μm) joins the cells with 6 solder joints (3 on each cell) as shown in Figure 4b.** Only the region around one of the solder joints as shown in **Figure 4c** was subjected to μSXRD as scanning the entire sample is very time-consuming and thus impractical considering the typical limited beam time allocation in synchrotron facilities**. The nominal thickness of the solder pad in the solder joint shown in Figure 4c is ~ 100 μm. However, it can be noticed that the solder is spread around the joint in small zone where the solder thickness varies from 100 μm to zero. Figure 4d shows typical back metallization lines (10 - 20 μm) thick on the silicon cell.** The same cells were later encapsulated in the solar PV laminator with a tempered front glass sheet and EVA encapsulation polymer at 150 °C and 1 bar (0.1 MPa) vacuum pressure. The approximate lamination recipe is shown in **Figure 4e** and the mini module thus fabricated is shown in **Figure 4f**. A portion of one of the cells was removed in order to fit the two-cell string into the mini module of size 200x200 mm as a bigger module could not be mounted on the μSXRD sample stage at the ALS beamline 12.3.2 of LBNL, Berkeley. **Figure 4g** shows the actual μSXRD scan region after encapsulation. It can be noticed that the region scanned before and after encapsulation is approximately the same. Furthermore, the back sheet was not used in the mini module as it blocks X-rays from reaching solar cells in the module.

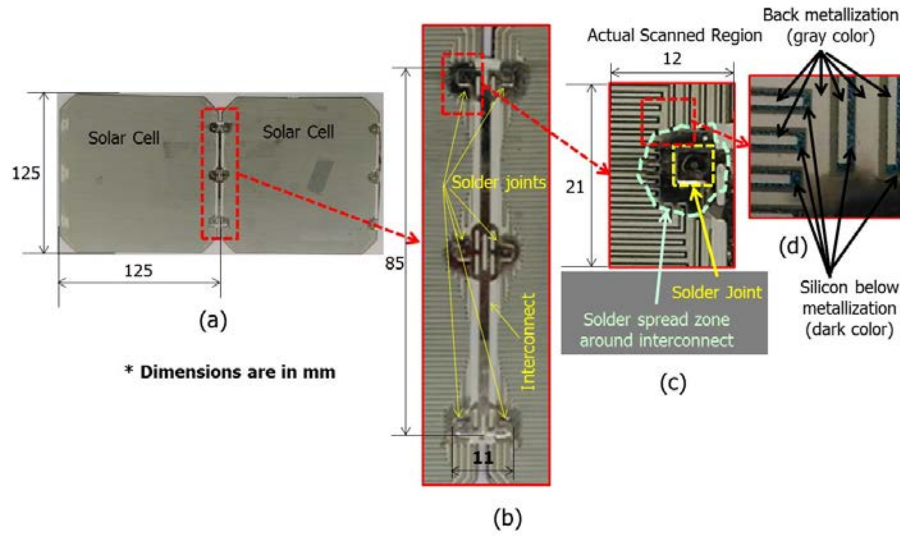

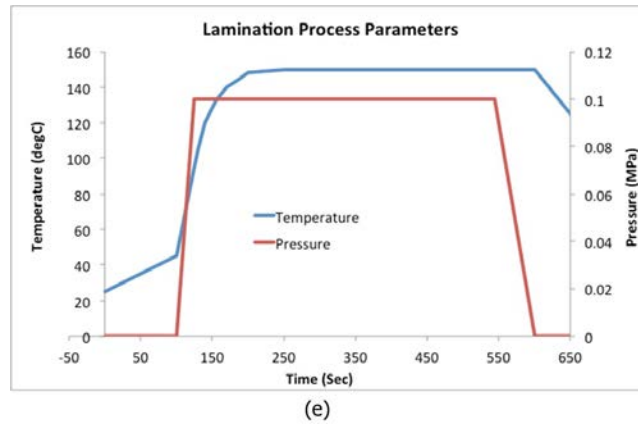

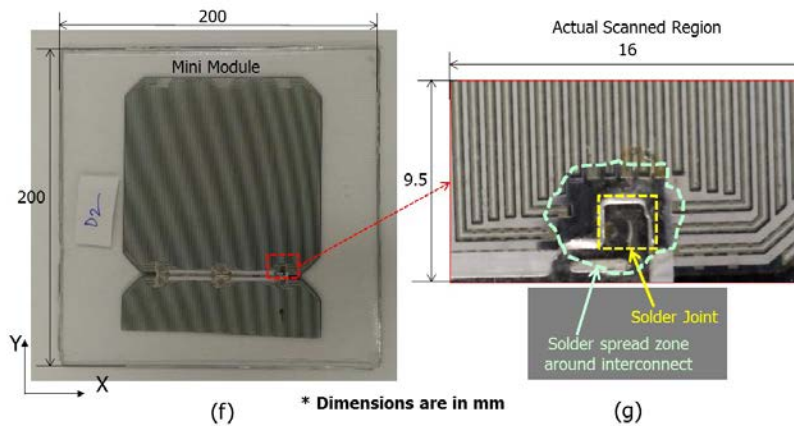

Figure 4: (a) Soldered string of two solar cells subjected to μSXRD, (b) Zoomed in picture of interconnect showing 6 solder joints, 3 with each cell, (c) Picture of actual scanned region with solder joint, (d) Zoomed in picture showing back metallization lines (10 - 20 μm thick) on the cell, (e) Lamination recipe (approximate), (f) Mini solar module (with same cell string) subjected to μSXRD, (g) Picture of actual scanned region after lamination

Figure 5a shows a schematic micro diffraction setup of the mini solar module and Figure 5b shows a picture of the actual setup. The sample was mounted on the stage with its back (metallization side of the solar cell) facing the X-ray beam. This is because X-rays can't penetrate the front glass due to absorption. The sample stage that is capable of moving in X, Y and Z directions was adjusted to focus the X-ray beam on the sample as required by the experiment. The sample lies in the XY plane and the Z direction is normal to the sample plane [26], so that movement in the XY plane do not break the focus of the X-ray beam. Then, both the samples were scanned using a 100μm displacement step along the X and Y directions.

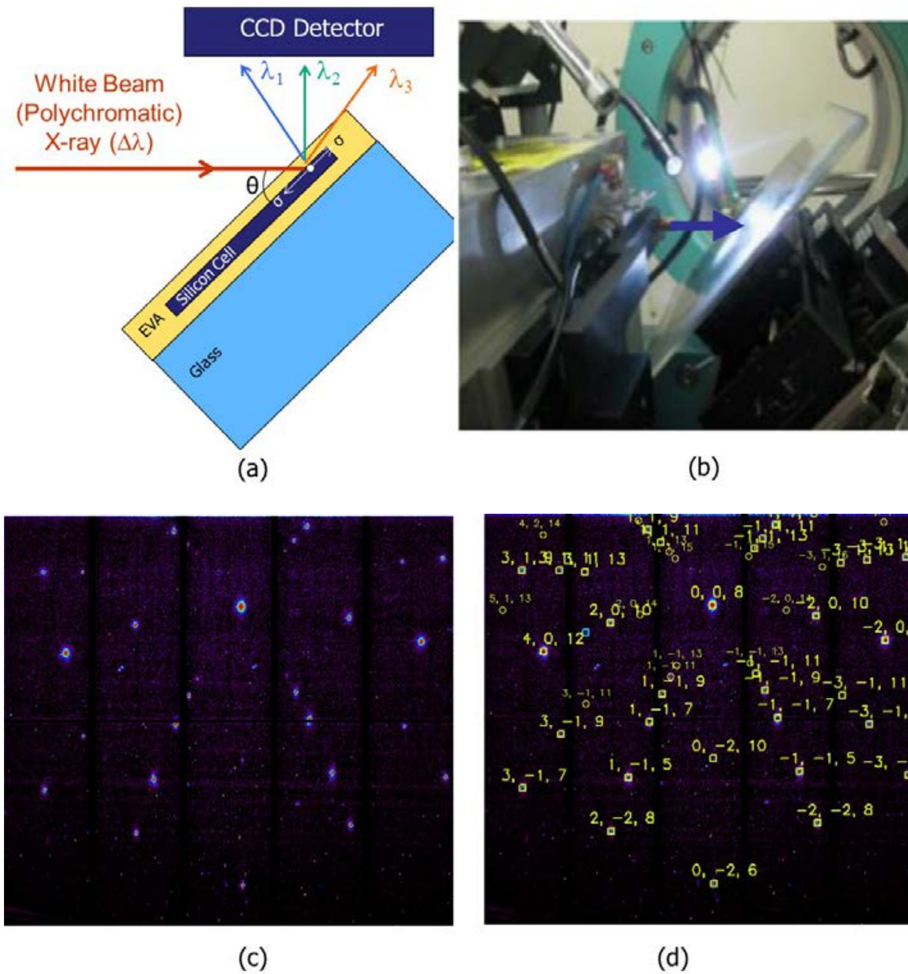

Figure 5: (a) Schematic of Solar Module μXRD Setup, (b) Actual picture of the Test Setup, (c) Typical Laue pattern before indexing, (d) Laue pattern after indexing.

A typical Laue diffraction pattern from the encapsulated solar cell sample before indexing was shown in Figure 5c and same pattern after manual indexing using XMAS program [26] was shown in Figure 5d. XMAS uses a peak fitting routine to calculate the crystal plane orientations of the diffraction peaks. The accuracy of the fit depends on the number of indexed peaks, hence we use all the peaks for analysis. The indexed Laue pattern in Figure 5c has 32 peaks and associated peak fit parameters was presented in Table 1. In general, there will be around 20 - 35 silicon

peaks in the typical Laue graph of the single crystal silicon cell in our analysis. It should be noted that the number of peaks depends on the position, area and sensitivity of the detector employed in the beamline. The no. of peaks decreases due to attenuation of X-ray beam due to the presence of obstacles such as back metallization, solder etc. In case of thin (10 -20 µm) back metallization, the intensity of the diffraction peaks from underlying silicon will be very low compared to bare silicon. In such a scenario, XMAS can still identify and index them using a routine called adaptive indexing. In adaptive indexing, the peak approximate positions corresponding to a grain (entire cell is 1 grain in single crystal silicon) will be identified by indexing the Laue pattern from bare silicon (where there is no back metallization) and then the known silicon peaks of very low intensity can be detected in case of Laue patterns from silicon below metallization. As a thumb rule, the scan point with Laue pattern having less than 20 indexed peaks will be treated as no signal (hence no result). In case of thicker obstacle such as solder joint/interconnect, the X-ray is completely blocked from silicon, practically giving no peaks at all.

Table 1: List indexed silicon peaks of the Laue pattern shown in Figure 5d (h k l are the miller indices of the diffracting plane)

Peak No.	h	k	l	Energy (keV)	2theta (deg)	intensity	Peak No.	h	k	l	Energy (keV)	2theta (deg)	intensity
1	0	0	8	13.04	88.90	1.05E+06	17	3	-1	9	18.81	70.74	2.25E+05
2	0	-2	6	16.43	52.14	4.81E+05	18	-1	-1	9	16.88	76.09	8.41E+05
3	4	0	12	21.98	82.16	1.05E+06	19	-3	-1	9	18.36	72.78	2.89E+05
4	-2	0	6	10.75	84.39	8.82E+05	20	-1	1	9	13.46	101.20	1.05E+06
5	1	-1	5	11.14	64.33	1.05E+06	21	1	1	9	13.55	100.29	1.05E+06
6	-1	-1	5	10.96	65.54	1.05E+06	22	3	1	9	14.95	93.49	6.55E+05
7	2	-2	8	19.89	58.29	4.23E+05	23	-3	1	9	14.66	95.93	4.90E+05
8	-2	-2	8	19.45	59.74	5.28E+05	24	-1	-1	11	20.02	78.48	1.20E+05
9	3	-1	7	16.35	64.89	7.98E+05	25	-3	-1	11	21.18	76.20	3.30E+04
10	1	-1	7	13.97	71.40	1.05E+06	26	-1	1	11	16.64	99.12	2.55E+05
11	-1	-1	7	13.81	72.36	9.43E+05	27	1	1	11	16.73	98.39	3.29E+05
12	-3	-1	7	15.81	67.36	5.10E+05	28	3	1	11	17.91	93.67	1.95E+05
13	0	-2	10	21.27	66.36	1.26E+05	29	-3	1	11	17.62	95.71	1.94E+05
14	2	0	10	17.07	86.03	9.75E+05	30	-1	1	13	19.84	97.64	3.87E+04
15	-2	0	10	16.84	87.47	7.92E+05	31	3	1	13	20.96	93.56	1.37E+04
16	1	-1	9	17.02	75.34	6.57E+05	32	-3	1	13	20.67	95.31	1.36E+04

The measured sequence of Laue patterns can be automatically analyzed by XMAS to obtain the corresponding crystal orientation and deviatoric stress tensor maps (Figure 3). However, the X-ray beam used penetrates all the way though the thickness of the silicon cell [27]. Therefore, the obtained maps show the average stress and orientation over the thickness of the cell at each point. **But the calculated stresses are actually weighted average over the thickness of the cell. We say weighted average, as the silicon outer surface facing the X-ray beam diffracts more than the inner silicon as the X-ray beam get attenuated while passing through the cell and the weight function is unknown. In such a scenario the accuracy of the deviatoric stress components directly calculated by XMAS is questionable. Moreover, bending of the cell is the major reason for stress, which get affected due to averaging over the cell thickness. Further, it was found that the shear stress components calculated by XMAS are prone to uncertainties due to uncertainties in the diffraction peak positions and associated geometric modeling [28]. Because of the above said reasons we didn't consider / present the deviatoric stress maps directly calculated from XMAS. Alternatively, we calculated the directional stress components in the plane of the solar cell, using the crystal plane mis-orientation angles.** The orientation of Si does not vary significantly though the depth of cell due to its small thickness (~ 180µm) compared to planar dimensions (125mm x125mm) and **hence**

the calculation is almost independent of the averaging diffraction signal across the cell thickness. Knowing the orientation map, the deformed shape of the cell in the scanned region can be calculated. Later it can be used to calculate the stress state in silicon using theory of thin plates **[29]** as explained in the following subsection.

2.3 Data Analysis (Residual Stress Evaluation)

The XMAS program automatically calculates the mis-orientation angles of the cell in the XZ plane, namely φ_y (bending around the Y-axis) and the YZ plane, and φ_x (bending around the X-axis). Using these angles, the local curvature of the cell about the X and Y axes, κ_{xx} and κ_{yy}, can be calculated **[29-31]** as shown in Figure 6 using equations (1) and (2). The negative sign in equation (1) is because the X-ray beam is fixed and the sample stage moves forward in the X-direction during XRD scanning, which is equivalent to beam travel in the opposite direction (negative X direction).

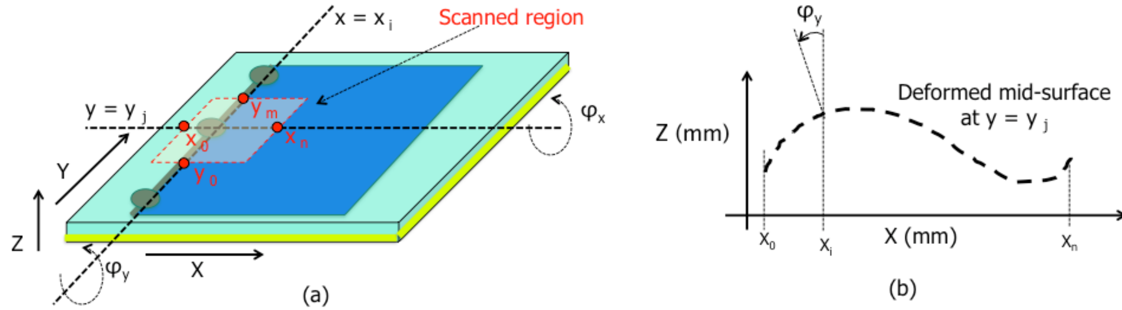

Figure 6: (a) Schematic of solar PV laminate, showing μSXRD scan region and it's orientation and associated crystal plane mis-orientation angles in XZ plane, φ_y and YZ plane, φ_x , (b) Schematic of calculation of local curvature using equations (1) and (2)..

$$\kappa_{xx} = -\frac{\partial \varphi_y}{\partial x}\bigg|_{y=const}, \ \varphi_y \text{ in radians} \quad (1)$$

$$\kappa_{yy} = \frac{\partial \varphi_x}{\partial y}\bigg|_{x=const}, \ \varphi_x \text{ in radians} \quad (2)$$

Once the local curvatures are calculated the respective bending strains on the surface of the cell can be calculated using the following assumptions similar to the ones used in the Kirchhoff plate model **[29]**.

- The cell is thin (thickness is much smaller than characteristic length: 180 μm ≪ ~156 mm);
- The cell thickness doesn't vary over the area of cell (*t* ~180μm);
- The cell is symmetric about the mid-surface (its neutral plane is equivalent to the mid-surface);
- All the loads are distributed over surface areas greater than *t*/2;
- There is no significant extension of the mid-surface in the regions, which are not covered by thick layer of solder (the layers are considered to be thin if the solder is significantly thinner than *t*).

Using the assumptions, bending strains on the surface of the cell can be calculated as shown in equations (3) and (4) below.

$\varepsilon_{xx} = -\frac{t}{2}\kappa_{xx}$, where '*t*' is thickness of the silicon cell and (3)

$$\varepsilon_{yy} = -\frac{t}{2}\kappa_{yy} \quad (4)$$

The strains can be used to calculate the stresses using Hooke's law. As the silicon cells in the samples are made of single crystalline silicon of <100> orientation (ie. the surface is the {100} plane), the anisotropic elastic tensor (component magnitudes in GPa) was used as shown in equation (5) **[32]**.

$$C = \begin{bmatrix} C_{11} & C_{12} & C_{13} & 0 & 0 & 0 \\ C_{21} & C_{22} & C_{23} & 0 & 0 & 0 \\ C_{31} & C_{32} & C_{33} & 0 & 0 & 0 \\ 0 & 0 & 0 & C_{44} & 0 & 0 \\ 0 & 0 & 0 & 0 & C_{55} & 0 \\ 0 & 0 & 0 & 0 & 0 & C_{66} \end{bmatrix} = \begin{bmatrix} 166 & 64 & 64 & 0 & 0 & 0 \\ 64 & 166 & 64 & 0 & 0 & 0 \\ 64 & 64 & 166 & 0 & 0 & 0 \\ 0 & 0 & 0 & 80 & 0 & 0 \\ 0 & 0 & 0 & 0 & 80 & 0 \\ 0 & 0 & 0 & 0 & 0 & 80 \end{bmatrix} \quad (5)$$

According to Hooke's law, using plane stress assumption and the assumptions above, the directional stresses in Si can be calculated as follows:

$$\sigma_{zz} = 0 \quad (6)$$
$$\sigma_{xx} = \left(C_{11} - \frac{C_{12}^2}{C_{11}}\right)\varepsilon_{xx} + \left(C_{12} - \frac{C_{12}^2}{C_{11}}\right)\varepsilon_{yy} \quad (7)$$
$$\sigma_{yy} = \left(C_{12} - \frac{C_{12}^2}{C_{11}}\right)\varepsilon_{xx} + \left(C_{11} - \frac{C_{12}^2}{C_{11}}\right)\varepsilon_{yy} \quad (8)$$

As explained in section 2.2, the thickness of the copper interconnect is 100 µm and the nominal thickness of the solder pad below interconnect is around 100 µm. So the solder joint is nominally 200 µm thick and there is a solder spread zone (Figures 4c and 4g) around the joint where the solder thickness varies from 100 µm to zero. It should be noted, that the X-ray penetration depth into solder is less than 150µm [27]. Hence, the maximum solder thickness where we can still get the scattered signal from Si is less than 75µm. Therefore, the equations above can be applied to calculate the stresses at any point where we can obtain the Laue pattern and orientation. The stress maps calculated using the experimental procedure are presented later in the results and discussion section.

3. Finite Element Modeling and Simulation

In the present study, both 2D and 3D finite element (FE) models have been developed to simulate the stress evolution in silicon cells. The 2D FE model is plane-strain approximation of a generic single cell module with a single interconnect, aimed at

elucidating the fundamental physics of residual stress evolution during PV module fabrication. The 3D FE model represents the experimental mini-module sample shown in Figure 4d and is aimed at a direct comparison with the experimental results. The details of both the FE models are presented in this section.

3.1 2D Finite Element Model

The 2D FE model is plane-strain approximation of a single back contact silicon cell mini module with a single interconnect solder joint as shown by the schematic in Figure 7a. **But it is very fundamental in nature as it models evolution of deformation and stress of a single silicon cell due to a single interconnect / solder joint during module integration process from soldering to encapsulation. Since the deformation of the cells after soldering is quite common in generic silicon solar cells [4-6], this 2D model is applicable to generic silicon solar cells as well. Actual FE model and mesh details are shown in Figure 7b. Solder between interconnect and the cell was not modeled in this simulation. All the materials used in the model were assumed to be isotropic and linearly elastic as shown in Table 2 [15-16, 32]. Linear elastic but temperature varying material properties was assumed in this simulation in order to understand the fundamental physics of the problem. Use of advanced material properties (such as viscoelasticity of encapsulation polymers) introduces too many parameters in the model and hence it would be difficult to explain the effect of more fundamental parameters such as elastic modulus and CTE (coefficient of thermal expansion) effectively. The advanced material properties can be implemented upon solid understanding of basic physics of the problem.**

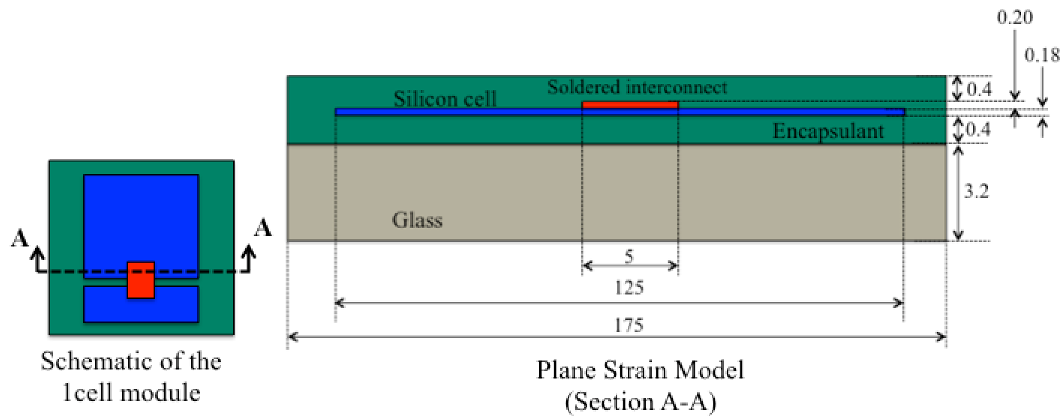

(a)

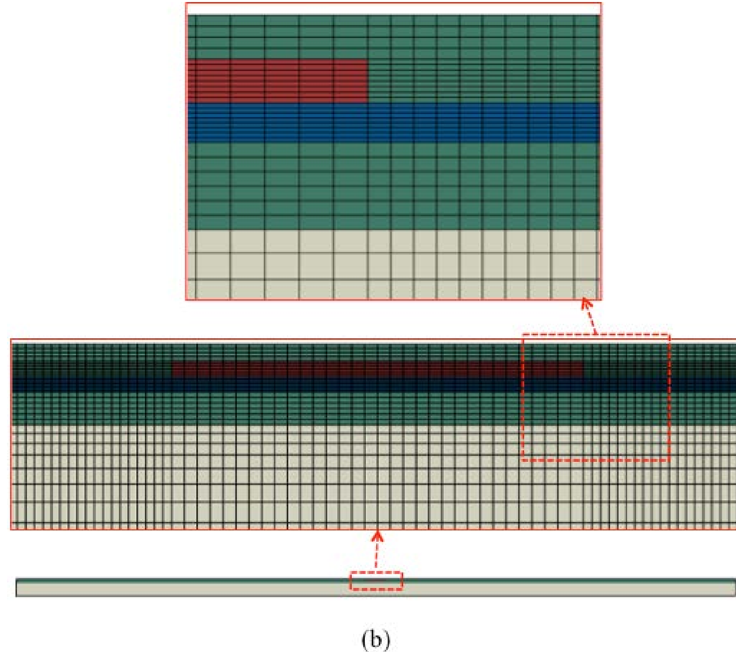

Figure 7: (a) Schematic of the 2D FE model showing dimensions of different components of the mini PV module in mm (not to scale), (b) Actual FE model with mesh details at interconnect region in the zoomed-in images.

The module integration process was simulated in 2 steps as explained below.

1. Cell-to-interconnect soldering: CTE mismatch from soldering temperature, 210 °C (actual soldering temperature is ~ 220 °C at which the solder will be in molten state) to room temperature, 25 °C. Only the cell and interconnect were present in this step of the simulation.
2. Module Lamination: The lamination process was simulated in the following 4 sub-steps based on the lamination recipe shown in **Figure 4e**.
    a. Preheating to 50 °C
    b. Vacuum pressure (0.1 MPa) application
    c. Heating to lamination temperature, 150 °C.
    d. Cooling to room temperature, 25 °C.

Steady state conditions were assumed in all the simulation steps and transient effects were not considered. The soldering step is important in the simulation as it simulates the initial bowing/bending of the silicon cell before lamination. During the lamination process, the bent cell is flattened by the vacuum pressure, leading to higher tensile stresses in the cell region near the interconnect. **The encapsulation polymer softens at elevated temperatures but it rather acts as a highly viscous adhesive and still is able to transfer the pressure load to the cells to flatten them. Further due to its high viscosity and adhesive nature, it also transfers the constraints from glass to the cells at high temperature and hence keeps them flattened even after the pressure was removed. This phenomenon was commonly observed and verified during PV module sample lamination process in our laboratory.**

The FE model was meshed with 4-node quadrilateral elements and mesh convergence was studied by decreasing the element size along the length of the cell while keeping the element size across the thickness of the cell constant (0.0225 mm). Converged results were obtained at an element size of ~ 0.1 mm along the cell length.

Table 2: Material Properties of Components used in the FE Model [15-16, 32]

Material	Young's Modulus, E (GPa)		Poisson's Ratio	CTE (mm/mm/deg C)	
	Value	Temperature (deg C)		Value	Temperature (deg C)
Silicon	130 (refer Eqn (5) for anisotropic elastic tensor, C)	---	0.28	1.72E-06	-53
				2.23E-06	-13
				2.61E-06	27
				2.92E-06	67
				3.34E-06	147
Copper (Interconnect)	91.5	-40	0.3	1.70E-05	---
	85.7	25			
	82	125			
	79.2	225			
Solder (Sn-Ag-Cu)	53	0	0.35	2.10E-05	---
	45	100			
	36	200			
Glass	73	---	0.235	8.00E-06	---
Encapsulant (EVA)	0.1	-20	0.4	2.70E-04	---
	0.0065	100			

3.2 3D Finite Element Model

The 2D FE model explained above provides fundamental understanding of the basic physics during module integration. However, a 3D FE model was further developed and analyzed in order to show a better correlation with the experimental results for the given design of PV module. The 3D FE model shown in Figure 8 is a numerical representation of the experimental sample (**Figure 4f**). The FE model was meshed with 8 node linear brick elements throughout the model and the mesh details are shown in Figure 9. The interconnect geometry was approximately modeled to keep the mesh size within limits. Solder tabs between interconnects and cells at all the 6 solder joints were modeled. Anisotropic stiffness (Eqn. 5) of silicon was considered in this simulation. Material properties of the components were taken from Table 2. Further in this simulation plasticity of the copper interconnect as shown in Table 3 [16] was considered to accommodate the stiffness changes of interconnect upon yielding during the process, which seemed to affect the cell out of plane deformation significantly. In this model the back metallization of the silicon cells was omitted as the design and process parameters of it were not available in the public domain and also incorporating such minute detail will make the FE model computationally expensive. **Similar to the 2D simulation, linear elastic but temperature varying material properties was assumed for solder and encapsulation polymer in the 3D simulation also to understand and explain the effect of more fundamental parameters such as elastic modulus and CTE on the cell residual stress effectively. Linear elastic and temperature varying material model for these materials are expected to serve as a good approximation to explain the fundamental physics and worst-case scenario at a lower computational expense.**

The simulation procedure followed was exactly same as the 2D FE model explained above and the results are discussed in the following section.

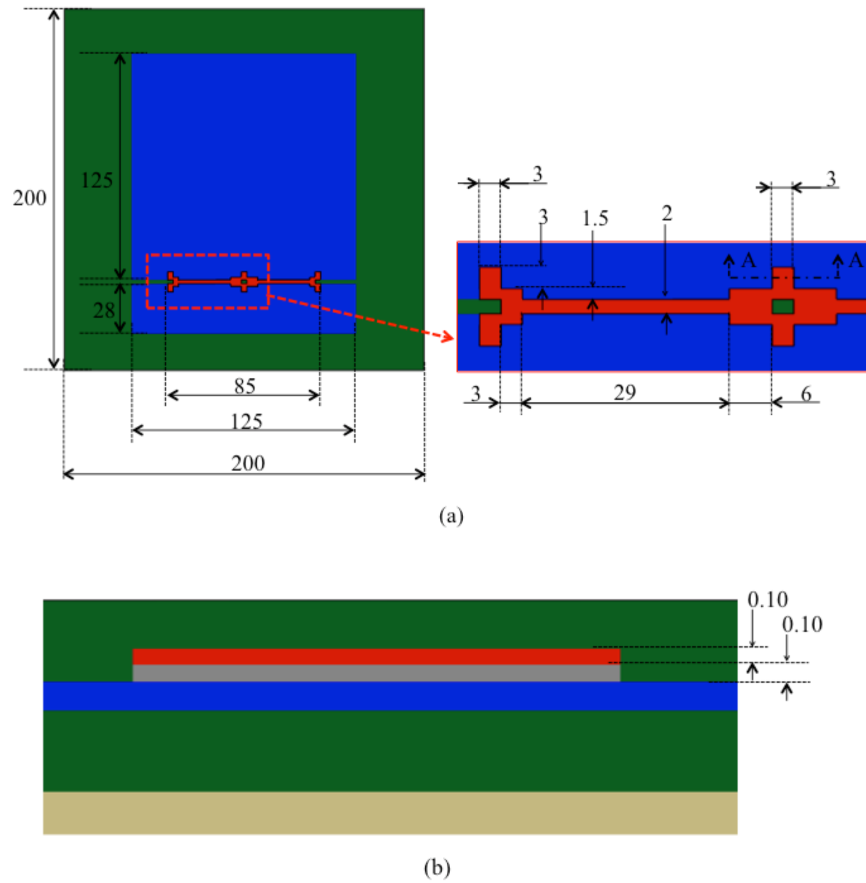

Figure 8: (a) 3D FE model, showing dimensions of different components of the sample PV module (the encapsulation layer over the cells and interconnect was removed from the picture to add clarity), (b) Cross-section of the model at mid portion of interconnect (Section A-A in a), showing interconnect and solder thicknesses. The thicknesses of the rest of the parts are the same as in the 2D FE model (Figure 7)

Table 3: Plastic properties of copper interconnect [16]

Yield Stress (MPa)	Tangent Modulus (MPa)	Temperature (deg C)
116.2	1000	-40
95.1	1000	25
82	1000	125
79.2	1000	225

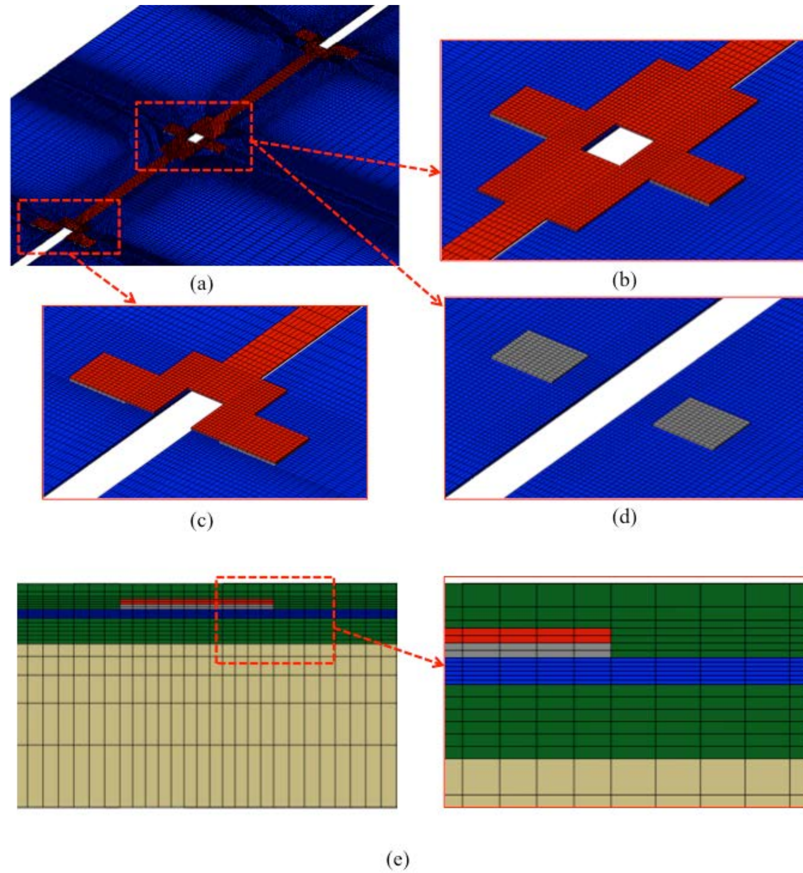

Figure 9: (a) Mesh details near interconnect of 3D FE model, (b) Mesh details around mid-portion of the interconnect, (c) Mesh details around end portion of the interconnect, (d) Mesh details below mid-portion of the interconnect showing solder pads, (e) Cross section showing mesh details across different layers of the model at mid-portion of interconnect (ref. section A-A in Fig 8a)

4. Results and Discussion

Synchrotron X-ray micro-diffraction has been used to evaluate the residual stresses in single crystalline silicon cells before and after encapsulation process. **The crystal plane mis-orientation maps of the scanned regions (Figure 4c and 4g) are shown in Figure 10. The gray regions in the mis-orientation maps indicate interconnect/thick solder layer, which the X-ray beam could not penetrate and hence no signal. These mis-orientations were the direct output of the experiment and the cell residual stresses were calculated as explained in section 2.3 using these mis-orientations. The corresponding stress maps are shown in Figure 11 (The white regions in the stress maps indicate interconnect/thick solder layer, which the X-ray beam could not penetrate and hence no signal). It is evident from the stress maps that the magnitude of the post-lamination residual tensile stress in the cell near the solder joint region is much higher than the post-solder residual stress. Comparing Figures 11a and 11c show that the maximum value of the tensile residual stress in X-direction after soldering (before lamination) is ~ 50 MPa, which increased to ~ 90 MPa after lamination. Similarly, in Y-direction the maximum value of the tensile residual stress**

after soldering (Figure 11b) is ~ 50 MPa, which increased to above 100 MPa after lamination (Figure 11d). This finding confirms that the local curvature of the cell in the vicinity of the solder joint indeed increases after the lamination process. However, these results cannot provide a physical reasoning for this behavior, which the finite element simulations can. **It can also be observed from Figures 11a and 11b that there is a large value of compressive residual stress (40 – 100 MPa) around the solder joint after soldering, which is due to the solder spread zone around the joint (Refer Figure 4c). However, after lamination, this compressive stress was relaxed to a smaller value or became tensile (Figures 11c and 11d) due to the change in local curvature of the cell.** Further we can notice that the effect of back metallization of the cell is very significant in the stress maps and it is higher in post-lamination stresses.

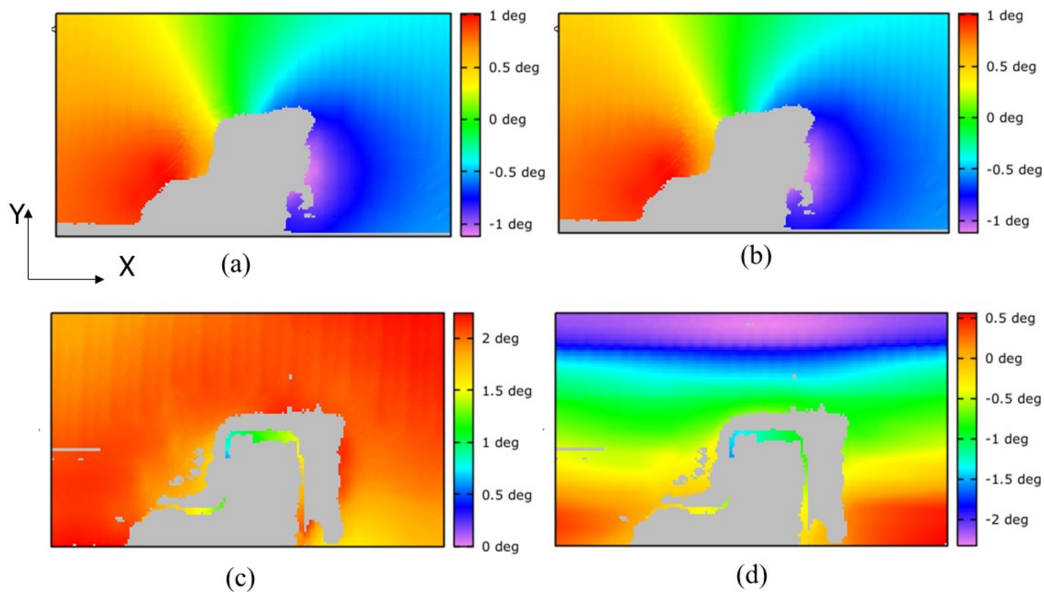

Figure 10: Crystal plane mis-orientation angles (deg) in the silicon cell from μSXRD, (a) Post-solder mis-orientation in XZ plane (φ_y), (b) Post-solder mis-orientation in YZ plane (φ_x), (c) Post-lamination mis-orientation in XZ plane (φ_y), (d) Post-lamination mis-orientation in YZ plane (φ_x). Note: gray regions inside the maps indicate interconnect/thick solder layer, which the X-ray beam could not penetrate and hence no signal

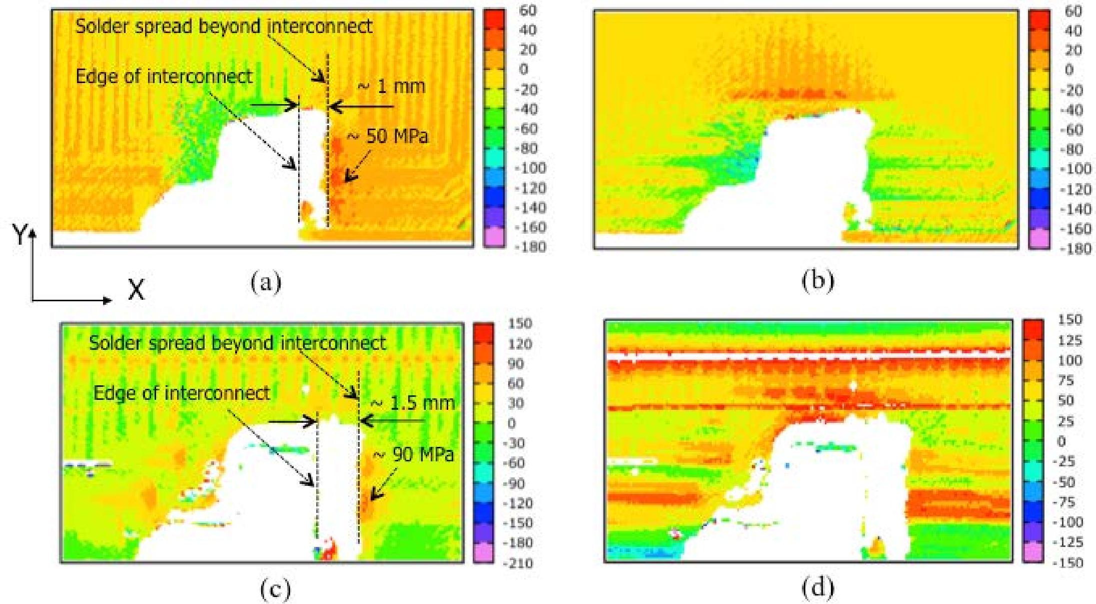

Figure 11: Residual stresses (MPa) in the silicon cell from μSXRD, (a) Post-solder residual stress in the X-direction, (b) Post-solder residual stress in the Y-direction, (c) Post-lamination residual stress in the X-direction, (d) Post-lamination residual stress in the Y-direction. Note: white regions inside the maps indicate interconnect/thick solder layer, which the X-ray beam could not penetrate and hence no signal

Displacement contours of the cell from the 2D FE simulation are shown in **Figure 12** and the corresponding residual stress contours along the cell in **Figure 13**. It can be noticed from **Figure 12a** that the cell below the interconnect was considerably warped post-soldering due to CTE mismatch and the rest of the cell was translated following the curvature of the cell below the interconnect. Consequently, the cell region interfacing the interconnect was in maximum compressive bending stress (~ -220 MPa) and the outer face of the cell was in maximum tensile bending stress (~ 90 MPa) as shown in **Figure 13a**. The cell region adjacent to the interconnect shows small tensile stress (~ 60 MPa) due to contraction of adjacent material (cell below interconnect). During lamination process the cell was forced to become flat by the interfacing material in the module as shown in **Figure 12b**. However highly localized cell deformations in the close vicinity of interconnect was observed (zoomed in image of **Figure 12b**) even after lamination process. **Physical reason behind this seemingly unreasonable deformation can be explained using the flexural stiffness. The flexural stiffness (characterized by the product of Young's modulus and moment of inertia, EI) of the soldered cell is not uniform. At the solder joint the flexural stiffness is different from rest of the cell due to the presence of the copper interconnect. Hence there is a jump of flexural stiffness at the edge of the interconnect as shown in Figure 12c. Further the compressively stressed silicon surface interfacing the interconnect can only partially relax when the bent cell becomes flat. This is due to the kinematic boundary condition imposed on it by the interconnect.** This localized deformation causes high bending stress in the cell, which is evident from the post-lamination residual stress contours along the cell (**Figure 13b**). The cell region adjacent to the interconnect is in maximum tensile bending stress around 300 MPa.

Since the increase of the stress is considerably high, this result is very significant and cannot be ignored. More importantly it unfolds actual physical phenomenon, leading to the raise of stress magnitude near the interconnect from soldering to lamination observed in the experimental results. Further it can also be noticed form this analysis that the main cause of stress is the localized bending around the cell during lamination process, which is resulted from the soldering induced deformation of the cell and hence it is important to consider the soldering process in the simulation of the PV module integration process to estimate the actual magnitude of the stress in the cells. Merely superposing the stresses from separate soldering and lamination process simulations will not be able to unfold this phenomenon.

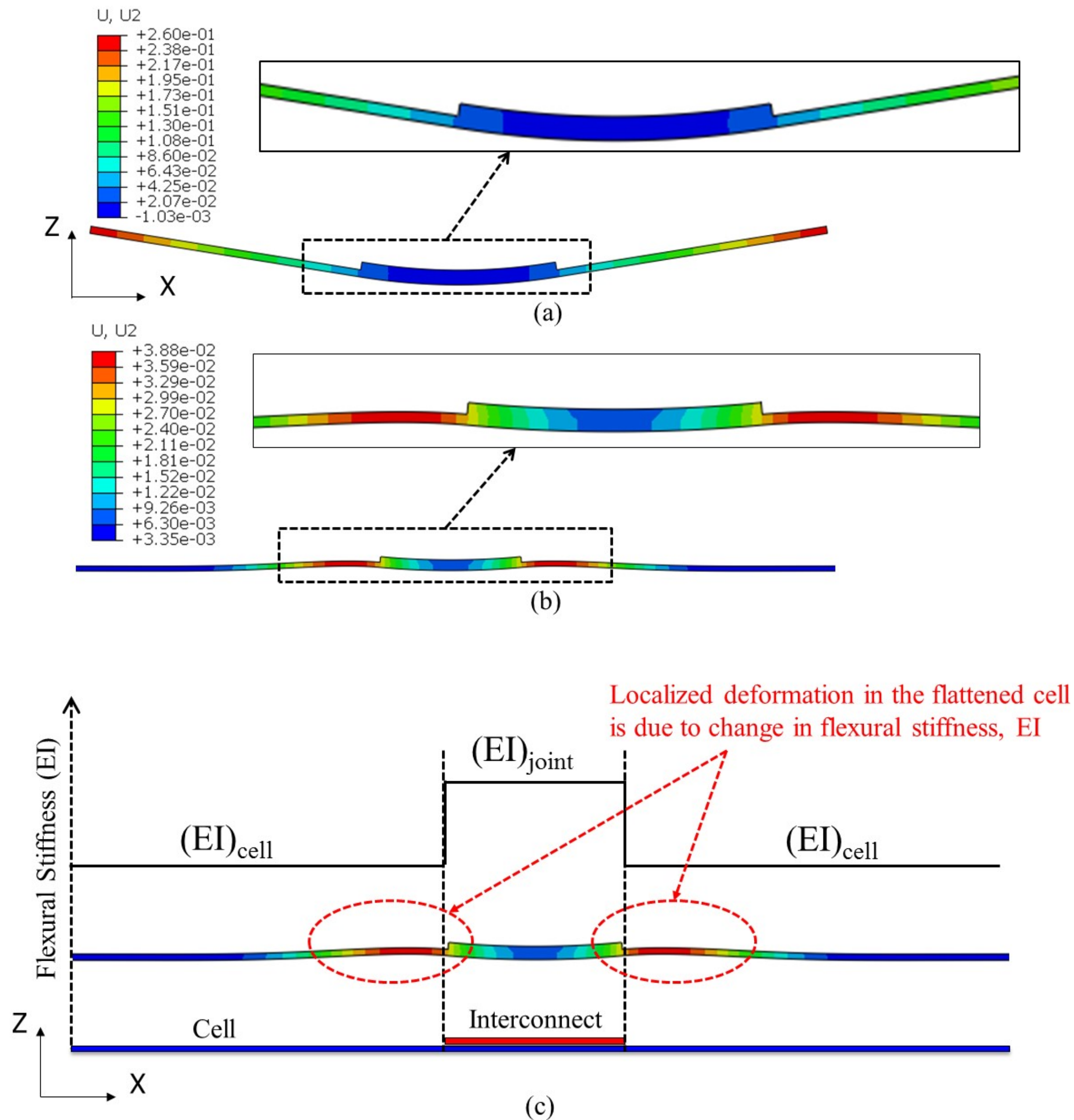

Figure 12: Vertical (Z-direction) displacement contours of silicon cell in mm, (a) Post-soldering Z-displacement (Scaled 5x), (b) Post-lamination Z-displacement (Scaled 5x, the other components have been removed for clarity and full length of the cell is not shown), (c) Schematic of the variation of flexural stiffness (EI) of the cell near the soldered interconnect.

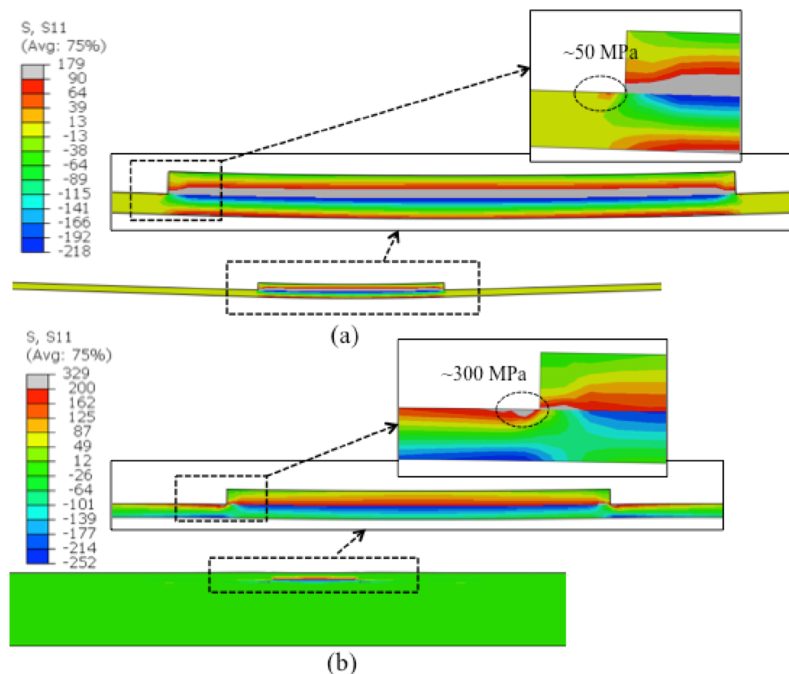

Figure 13: Residual stress contours along the cell in MPa (a) Post-soldering, (b) Post-lamination (only cell and interconnect are shown in zoomed-in plots)

Figures 14 and 15 show the displacement and stress contours in the cell from the 3D FE simulation. These results confirm the 2D FE analysis results and also can be directly compared with the experimental results. In order to make the comparison more meaningful, stress contours were shown only for the region of μSXRD scan so that the regions match geometrically. Comparing the stress maps from the μSXRD (**Figure 11**) and stress contour from the FE analysis (**Figure 15**) show that they are in good agreement, especially in terms of the high stress regions and overall behavior of the stress. Magnitudes of stresses as obtained in the simulation are different form the experimental values because of the simplifications used in the FE analysis such as idealized solder joint geometry, omitting back metallization and approximate material properties.

It can be noticed from **Figures 15a and 15c** that the maximum of X-direction stress (along the interconnect) in the cell is occurring right at the edge of the solder joint. And the corresponding region in experimental stress maps **(Figures 11a and 11c**) has no stress value. This is because in the actual sample (**Figures 4c and 4g**), solder was spread around the interconnect, blocking the X-ray. Hence comparison of peak values is not appropriate in this case. Alternatively, a comparison of X-direction stress magnitude at the edge of the solder zone in the experimental stress maps (refer markings **in Figures 11a and 11c**) with the corresponding regions in the FEA stress contours (refer markings in **Figures 15a and 15c**) showed very good agreement of stress magnitudes as well.

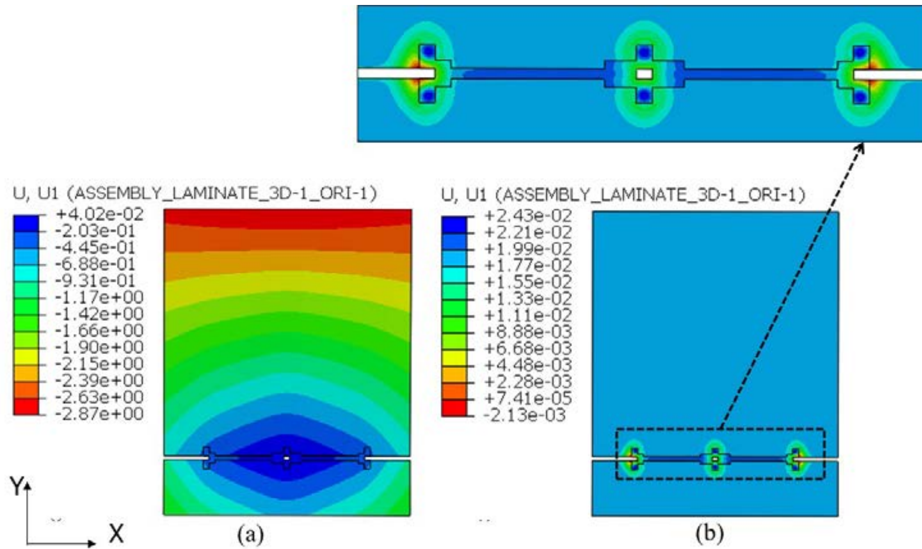

Figure 14: Vertical (Z-direction) displacement contours of silicon cell in mm, (a) Post-soldering Z-displacement, (b) Post-lamination Z-displacement. Note: the other Components have been removed for clarity.

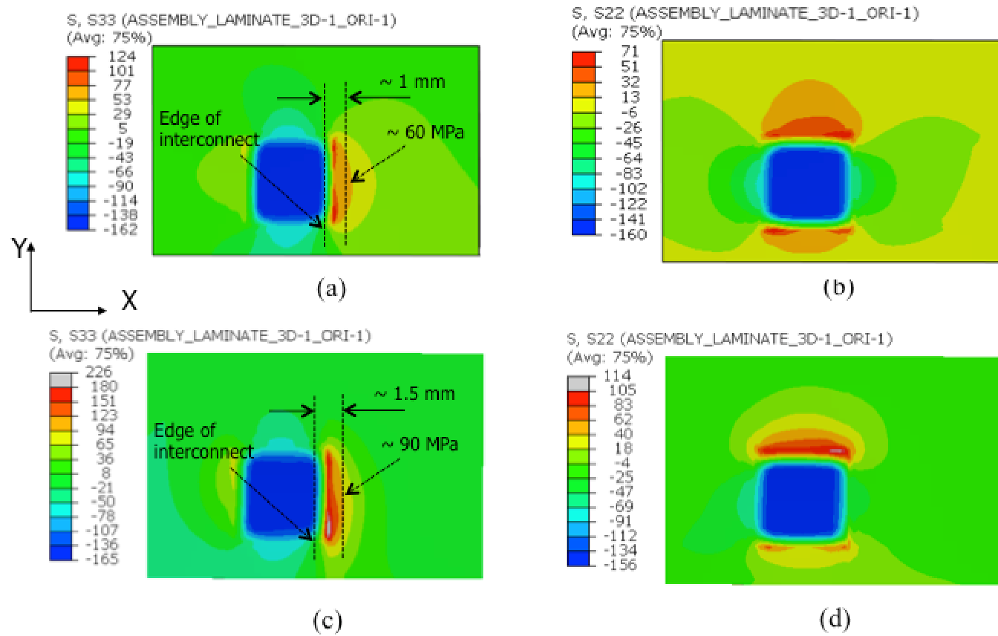

Figure 15: Residual stresses (MPa) in the silicon cell from 3D FEA, (a) Post-solder residual stress in X-direction, (b) Post-solder residual stress in Y-direction, (c) Post-lamination residual stress in X-direction, (d) Post-lamination residual stress in Y-direction

Back metallization of the silicon cells was omitted in this analysis as the design and process parameters of it were not available in the public domain and also incorporating such minute detail will make the FE model computationally expensive.

Further, we notice that the high stress in the cell under back metallization is concentrated close to the solder joint. Hence it can be attributed to the increased cell local curvature near the solder joint. As the back metallization tend to resist the local curving of the cell, a high stress will be induced in it. In such a case, we believe that the physics behind the high stress in the cell was adequately captured in our model even without the back metallization. Bulk of the back metallization lines was aligned with Y-direction (perpendicular to the interconnect) and they are expected to show higher influence on Y-direction stress. The same can be noticed from the experimental stress maps (**Figures 11b and 11d**), especially in the post lamination state. Therefore, the post lamination Y-direction stress magnitudes in experiment are not comparable with those of FEA (**Figure 15d**). But it can be noticed that the high stress zones are still matching well, leaving aside the metallization influence. Hence, the stress field in the vicinity of the interconnect solder joint is showing the same behavior and trend.

This model can be extremely useful as a tool to evaluate the effects of thinning silicon wafer, different encapsulation materials on the residual stress and fracture initiation locations in the encapsulated solar cells. **The experimentation, though very effective and accurate, cannot be performed on a large number of samples due to limitation of time and resources, our validated FE model can also serve as a tool to down select the critical samples (material / process combinations) which need to be tested for higher impact.** Methodologies can then be suggested to reduce residual stress and cell cracking, which are the subjects of our continued investigations.

5. Conclusions

Mechanical stress and fracture are the origins of failures of the solar PV cells during their fabrication as well as their operation in the field. Thus it is very important to have the tools to characterize them in a more quantitative manner. Through the studies in this article, μSXRD was used for residual stress evaluation in soldered and encapsulated solar cells. This tool has been proved to be a very useful technique with unique capabilities to characterize stress quantitatively and perhaps the only practical technique that could characterize the stress in encapsulated silicon solar cells.

Further in this work, the fundamental physics of the residual stress evolution in the silicon solar cells was explained by virtue of FE analysis. The local cell curvature near the solder joint has been found to be the actual reason for high residual stress after encapsulation, the most important result of this work, which was not reported so far. This explains the reason why the residual stress in encapsulated cells is considerably higher than that of the soldered cells (before encapsulation). The results obtained using the 3D FE simulations conform this observation and also demonstrate a good agreement with results of μSXRD. **Furthermore, the 2D FE model, which was actually used to demonstrate the localized bending with a silicon cell and single busbar (interconnect) is very generic in nature and not limited to any specific solar cell technology. Since the deformation of the cells after soldering is quite common [4-6] in generic silicon solar cells also, our 2D model is well applicable to generic silicon solar cells.**

Further experiments such as in-situ and in-operando evaluation of the solar cell modules can be devised using this technique to get a complete understanding of the stress evolution and fracture initiation of the solar cells in PV modules. The FE analysis methodology can be extended to perform thermal cycling and mechanical loading of the modules to completely characterize the stresses experienced by the cells in the module life cycle and fatigue life can be estimated. Further the FE simulations can also be used to perform sensitivity analysis to evaluate effect of different materials, geometrical and process parameters on the residual stresses in the solar cells. **The accuracy of the FE simulations can be further improved by using advanced nonlinear material models, especially for the encapsulation polymers.**

Finally, the results (both experimental and simulations) presented in this work characterize the silicon residual stresses resulted from the PV module integration process near the solder joints in the silicon cells, the current knowledge gap. Since the residual stresses in the cells are highly localized and possibly act as fracture initiation sources, the results presented here are believed to be very useful as they address such crucial knowledge gap and help the PV industry to resolve the existing module reliability issues.

Acknowledgements

The authors would like to thank for critical discussion with Solar Energy Research Institute (Singapore), SunPower Corporation (USA) and REC Solar (Singapore).

The authors gratefully acknowledge the samples and support provided by Dr. Alexander Caldwell of SunPower for the Synchrotron X-ray micro-diffraction experiments. Critical support and infrastructure provided by Singapore University of Technology and Design (SUTD) and Surya University (Indonesia) during the manuscript preparation is highly appreciated.

S. K. Tippabhottla, V.Handara, and A.S. Budiman also gratefully acknowledge the funding and support from National Research Foundation (NRF)/Economic Development Board (EDB) of Singapore for the project under EIRP Grant **"(NRF2013EWT- EIRP002-017) - Enabling Thin Silicon Technologies for Next Generation, Lower Cost Solar PV Systems**"

The Advanced Light Source (ALS) (supported by the Director, Office of Science, Office of Basic Energy Sciences, and Materials Sciences Division, of the U.S. Department of Energy under Contract No. DEAC02-05CH11231 at Lawrence Berkeley National Laboratory and University of California, Berkeley, California). The move of the micro-diffraction program from ALS beamline 7.3.3 onto to the ALS super-bend source 12.3.2 was enabled through the NSF grant #0416243.

References

[1] M. Sander, S. Dietrich, M. Pander, S. Schweizer, M. Ebert, and J. Bagdahn, “Investigations on crack development and crack growth in embedded solar cells”, Proceedings of SPIE –The International Society for Optical Engineering, 2011.
[2] I.J. Bennet et al., “Low-Stress Interconnection of Solar Cells”, 22nd European Photovoltaic Solar Energy Conference and Exhibition, Milan, Italy, 3-7 september2007.
[3] Pingel S, Zemen Y, Geipel T, Berghold J. Mechanical stability of solar cells within solar panels. Proc. 24th European Photovoltaic Solar Energy Conf., Hamburg, Germany; 2009, pp. 3459-3463.
[4] M. Gabor et al., Soldering induced damage to thin Si solar cells and detection of cracked cells in modules. 21st European Photovoltaic Solar Energy Conference, 2006.
[5] J. Wendt, M. Träger, M. Mette, A. Pfennig, B. Jaeckel, The link between mechanical stress induced by soldering and micro damages in silicon solar cells, in: Proceedings of EUPVSEC, 2009, pp. 3420–3423.
[6] Chih-Hung Chen et al., “RESIDUAL STRESS AND BOW ANALYSIS FOR SILICON SOLAR CELL INDUCED BY SOLDERING”, (http://140.116.36.16/paper/c38.pdf).
[7] S. Dietrich, M. Pander, M. Sander, and M. Ebert. “Mechanical investigations on metallization layouts of solar cells with respect to module reliability”, Energy Procedia 38 (2013) 488 – 497
[8] Guohui Sun et al., “Analytical Model of Thermal Stress for Encapsulation and Service Process of Solar Cell Module”, Advanced Materials Research Vols. 97-101 (2010) pp 2699-2702.
[9] Y. Lee and A.A. O. Tay. Finite thermal analysis of a solar photovoltaic module. 37th PVSC conf., Seattle, 19-24 June 2011.
[10] Y. Lee and A.A. O. Tay, Stress Analysis of Silicon Wafer Based Photovoltaic Modules in Operation", PV Specialist Conference, Austin, 3-8 June 2012.
[11] M. Sander, S. Dietrich, M. Pander, M. Ebert, and J. Bagdahn. Systematic investigation of cracks in encapsulated solar cells after mechanical loading. *Solar Energy Materials & Solar Cells*, 111:82–89, 2013.
[12] S. Dietrich, M. Pander, R. Meier, S.-H. Schulze, M. Ebert, MECHANICAL ISSUES ON SOLAR MODULES AND ENCAPSULATED COMPONENTS, PVMRW 2011
[13] Pander, M. Fraunhofer, Dietrich, S., Schulze, S.-H., Eitner, U., Ebert, M., Thermo-mechanical assessment of solar cell displacement with respect to the viscoelastic behaviour of the encapsulant, IEEE 2011
[14] S. Dietrich, M. Pander, M. Sander, S.H. Schulze, and M. Ebert. Mechanical and Thermo-Mechanical Assessment of Encapsulated Solar Cells by Finite-Element-Simulation. Proceedings of SPIE –The International So- ciety for Optical Engineering, 2008.
[15] Ulrich Eitner, Thermomechanical Analysis of Photovoltaic Modules, PhD Thesis, Centre for Engineering Sciences, Martin Luther University of Halle-Wittenberg, Germany, 2011.
[16] Osama Hassan et al., “Finite Element Modeling, Analysis, and Life Prediction of Photovoltaic Modules” J. of Solar Energy Engg., Transcations of the ASME, Vol.136,MAY2014.
[17] A.S. Budiman et al., “Enabling thin silicon technologies for next generation c- Si solar PV renewable energy systems using synchrotron X-ray microdiffraction as stress and crack mechanism probe” Solar Energy Materials & Solar Cells, 2014, Vol. 130, pp. 303-308.
[18] A.S. Budiman, “Enabling Thin Silicon Technology”, Science Highlights, June 2013, Lawrwnce Berkeley National Laboratory (www- als.lbl.gov/index.php/science-highlights/industry-als/829-improving- thin-silicon-solar-cell-technology.html).
[19] Sasi Kumar Tippabhotla, Ihor Radchenko, Karthic Narayanan Rengarajan, Gregoria Illya, Vincent Handara, Martin Kunz, Nobumichi Tamura, Arief Suriadi Budiman, “Synchrotron X-ray Micro-diffraction – Probing Stress State in Encapsulated Thin Silicon Solar Cells”, Procedia Engineering, Volume 139, 2016, Pages 123-133.
[20] Cullity, B. D. (1978). Elements of X-ray diffraction. 2nd edition. Addison-Wesley: New York.
[21] Brent Fultz · James Howe, Transmission Electron Microscopy and Diffractometry of Materials, 3rd Ed., Springer, 2007
[22] A.S. Budiman, Probing Crystal Plasticity at the Nanoscales, Springer, 2015.
[23] Kunz, M., Tamura, N., Chen, K., MacDowell, A. A., Celestre, R. S., Church, M. M., ... & Morrison, G. Y. (2009). A dedicated superbend X-ray microdiffraction beamline for materials, geo-, and environmental sciences at the advanced light source. Review of Scientific Instruments, 80(3), 035108.
[24] N. Tamura, M. Kunz, K. Chen, R. S. Celestre, A. A. MacDowell, and T. Warwick. A superbend X-ray microdiffraction beamline at the advanced light source. Materials Science and Engineering A-structural Materials Properties Microstructure and Processing, 524:28–32, 2009.
[25] N. Tamura, H. A. Padmore, and J. R. Patel. High spatial resolution stress measurements using synchrotron based scanning X-ray microd- iffraction with white or monochromatic beam. Materials Science and Engineering A-structural Materials Properties Microstructure and Pro- cessing, 399:92–98, 2005.
[26] Tamura N., XMAS: A Versatile Tool for Analyzing Synchrotron X-ray Microdiffraction Data, Chapter-4 of Strain and Dislocation Gradients from Diffraction, World Scientific, 2014.

[27] http://henke.lbl.gov/optical_constants/atten2.html
[28] A. Poshadel et al., Assessment of deviatoric lattice strain uncertainty for polychromatic X-ray microdiffraction experiments, J. Synchrotron Rad. (2012). 19, 237–244.
[29] S. Timoshenko, S. W. Krieger, Theory of Plates and Shells, 2nd ed., 1959.
[30] K. Chen, N. Tamura, W. Tang, M. Kunz, Y.C. Chou, K.N. Tu, Y.S. Lai, High precision thermal stress study on flip chips by synchrotron polychromatic X- ray microdiffraction, J. Appl. Phys. 107 (2010) 063502.
[31] M. A. Brown et al., A Comparison of X-Ray Microdiffraction and Coherent Gradient Sensing in Measuring Discontinuous Curvatures in Thin Film: Substrate Systems, J. of Applied Mech., Transcations of the ASME, Vol.73, pp. 723-729, Sep2006.
[32] Ville Kaajakari, http://www.kaajakari.net/~ville/research/tutorials/elasticity_tutorial.pdf (Last accessed May 2016).
[33] Zhanli Guo et al., Modeling Material Properties of Lead-Free Solder Alloys, J. of Electronic Mat., Vol. 37, No. 1, 2008.